Three-dimensional oceanic eddy analysis in the Southern California Bight from a numerical product

Changming Dong, Xiayan Lin, Yu Liu, Francesco Nencioli, Yi Chao, Yuping Guan, Dake Chen, Tommy Dickey, James C. Mcwilliams

Three-dimensional oceanic eddy analysis in the Southern California Bight from a numerical product

Changming Dong,[1] Xiayan Lin,[2,3] Yu Liu,[2,3] Francesco Nencioli,[4] Yi Chao,[5,6] Yuping Guan,[2] Dake Chen,[7] Tommy Dickey,[8] and James C. McWilliams[1]

Received 1 June 2011; revised 2 November 2011; accepted 6 November 2011; published 7 January 2012.

[1] With eight islands, complex coastlines and bottom topography, strong wind curls, and frequent upwelling fronts, the Southern California Bight (SCB) is an area with strong eddy activity. By applying an automated eddy detection scheme to a 12 year high-resolution numerical product of the oceanic circulation in the SCB, a three-dimensional eddy data set is developed. It includes information for each eddy's location, polarity, intensity, size, boundary, and moving path at nine vertical levels. Through a series of statistical analyses applied to the eddy data set, three-dimensional statistical characteristics of mesoscale and submeoscale eddy variations in the SCB are elucidated; these shed light on how eddies are generated, evolve, and terminate. A significant percentage of eddies is found to be generated around islands and headlands along the coastline, which indicates that islands in the SCB play a vital role in eddy generation. Three types of eddies, based on shape, are identified from the numerical product: bowl, lens, and cone. A dynamic analysis shows that some submesoscale eddies with finite local Rossby numbers tend to be ageostrophic balanced while mesoscale eddies are in geostrophic balance. The present research results are useful for the interpretation of data sets obtained during the interdisciplinary Santa Barbara Channel Radiance in a Dynamic Ocean (RaDyo) field experiment conducted on September 3–25, 2008.

Citation: Dong, C., X. Lin, Y. Liu, F. Nencioli, Y. Chao, Y. Guan, D. Chen, T. Dickey, and J. C. McWilliams (2012), Three-dimensional oceanic eddy analysis in the Southern California Bight from a numerical product, *J. Geophys. Res.*, *117*, C00H14, doi:10.1029/2011JC007354.

1. Introduction

[2] The Southern California Bight (hereafter referred to as SCB) is an oceanic region generally described to be south of Point Conception, north of San Diego, and east of the Santa Rosa Ridge (see Figure 1). Under a persistent positive wind stress curl in the SCB [*Winant and Dorman*, 1997], the low-frequency sea surface circulation in the SCB, is characterized by a domain-scale cyclonic gyre, or so-called Southern California Eddy [*Schwartzlose*, 1963]. It is composed of two branches: one is a broad, slow, and equatorward California Current carrying fresh and cold northern Pacific water toward the SCB, turning eastward into the Bight near its southern end; another is a poleward Southern California Countercurrent near the coast with warmer and saltier water advected from the tropics. Beneath the surface (at depths of 100–300 m), the coastal flow is dominated by a poleward California Undercurrent (CU). The low-frequency circulation pattern has been documented by numerous observational and numerical studies [*Hickey*, 1979, 1998; *Lynn and Simpson*, 1987, 1990; *Bray et al.*, 1999; *Harms and Winant*, 1998; *Dever et al.*, 1998; *Oey*, 1999; *Hickey et al.*, 2003; *Di Lorenzo*, 2003; *Oey et al.*, 2004; *Dong and Oey*, 2005; *Dong et al.*, 2009a].

[3] For the intraseasonal-scale (i.e., eddy-scale) variation, what we know is scarce in the SCB. With the existence of eight islands, complexity in the coastline, and fronts associated with frequent upwelling events, however, the SCB has strong eddy activity. *DiGiacomo and Holt* [2001] reported numerous eddies in the SCB using high-resolution Synthetic Aperture Radar (SAR) imagery, most of which are less than 30 km in diameter. Using high-frequency (HF) radar data, *Beckenbach and Washburn* [2004] have identified fine structures in the surface currents near the coasts in the northern part of the SCB. In the southern part of the SCB, near San Diego, *Kim* [2010] applied an eddy detection scheme to the HF radar-derived

[1]Institute of Geophysics and Planetary Physics, University of California, Los Angeles, California, USA.
[2]State Key Laboratory of Tropical Oceanography, South China Sea Institute of Oceanology, Chinese Academy of Sciences, Guangzhou, China.
[3]Also at Graduate University of the Chinese Academy of Sciences, Beijing, China.
[4]Laboratoire d'Océanographie Physique et Biogéochimique, UMR-CNRS-IRD 6535, Centre d'Océanologie de Marseille, Université de la Méditerranée, Marseille, France.
[5]NASA Jet Propulsion Laboratory, California Institute of Technology, Pasadena, California, USA.
[6]Also at Joint Institute for Regional Earth System Science and Engineering, University of California, Los Angeles, California, USA.
[7]State Key Laboratory of Satellite Oceanic Environment Dynamics, SIO/SOA, Hangzhou, China.
[8]Department of Geography, University of California, Santa Barbara, California, USA.

0148-0227/12/2011JC007354

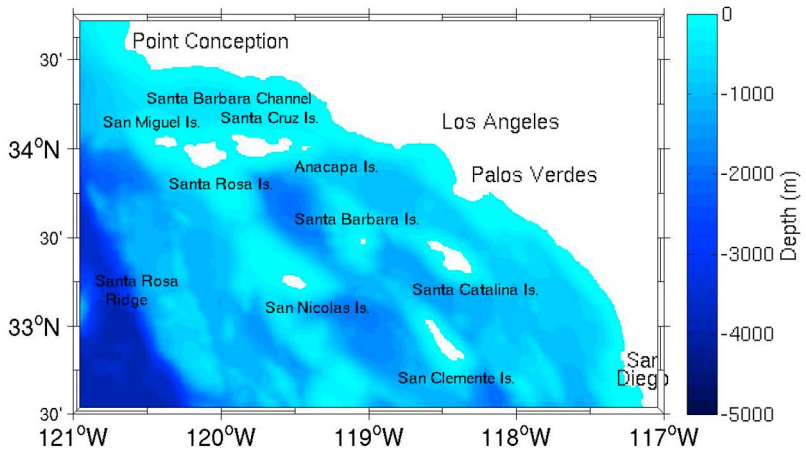

Figure 1. The numerical model domain. The color denotes the water depth.

surface current data and obtained an eddy data set. Based on in situ and remotely sensed measurements and numerical modeling, *Caldeira et al.* [2005] suggests that island wakes represent a mechanism for generation of the submesoscale eddies. To further understand the eddy generation and evolution processes in island wakes, *Dong and McWilliams* [2007] applied a high-resolution (1 km in its horizontal resolution) numerical model to study island wakes in the SCB. The model shows that eddies in lee sides of islands are generated by either an oceanic current passing islands or oceanic response to the wind wake due to the wind passing over the islands. Using the same model as *Dong and McWilliams* [2007], *Dong et al.* [2009a] integrates the model for eight-year (1996–2003) and makes extensive verifications against observational data available including satellite remote sensing, HF radar, and in situ data. The eight-year numerical solution suggests that the circulation in the SCB has multiple-scale variations. Its surface eddy variation is in an inter-annual variation and is in phase with the variation in the sea surface wind curl.

[4] Most of the former eddy studies in the SCB are focused on the sea surface and little is known about the vertical structures of eddies in the region. In this paper, we apply a high-resolution numerical product used by *Dong et al.* [2009a] to study three-dimensional eddy structures and variations (the product has been extended to 2007 and so the numerical product covers 12 years from 1996 to 2007). First of all, an eddy data set is set up by identifying mesoscale and submesoscale (i.e., smaller than the first baroclinic deformation radius) eddies from the numerical product and then statistical analysis is applied.

[5] The rest of the paper is composed of five sections: Section 2 describes the 12-year high-resolution numerical product. Section 3 briefly introduces an eddy detection and tracking scheme used and an approach to construct three-dimensional eddy structures. In section 4 a series of statistical analysis is applied to an eddy data set identified from the numerical product using the eddy detection scheme. Section 5 emphasizes the eddy analysis in the Santa Barbara Channel (SBC) region during September when the Radiance in a Dynamic Ocean (RaDyO) experiment conducted (T. Dickey et al., Introduction to special section, manuscript in preparation, 2012). Section 6 concludes the paper with discussions and summary.

2. The Numerical Product

2.1. Description

[6] The numerical product used in this study is generated using the Regional Oceanic Modeling System (ROMS). The ROMS solves the rotating primitive equations [*Shchepetkin and McWilliams*, 2005] with a generalized sigma-coordinate system in the vertical direction and curvilinear grid in the horizontal plane. A third-order, upstream-biased advection operator allows the generation of steep gradients in the solution, enhancing the effective resolution of the solution for a given grid size when the explicit viscosity is small. The numerical diffusion implicit in the third-order upstream-biased operator allows the explicit horizontal viscosity to be set to zero without excessive computational noise or instability. The vertical eddy viscosity is parameterized using a K-profile parameterization (KPP [*Large et al.*, 1994]).

[7] The model is configured in three levels of nested grids with the parent grid covering the whole U.S. West Coast. The first so-called child grid covers a large southern domain, and the third grid zooms in on the SCB region. The three horizontal grid resolutions are 20 km, 6.7 km, and 1 km, respectively. The external forcings are momentum, heat, and freshwater flux at the surface and adaptive nudging to gyre-scale SODA reanalysis fields [*Carton et al.*, 2000a, 2000b] at the boundaries. The momentum flux is derived from a three-hourly reanalysis mesoscale MM5 [*Grell et al.*, 1995] wind product with a 6 km resolution for the finest grid in the SCB. The oceanic model starts in an equilibrium state from a multiple-year cyclical climatology run, and then it is integrated from years 1996 through 2007. The first eight-year simulation at the 1 km resolution has analyzed and compared with extensive observational data collected: High-Frequency (HF) radar, current meters, Acoustic Doppler Current Profilers (ADCP), hydrographic measurements, tide gauges, drifters, altimeters, and radiometers [see *Dong et al.*, 2009a]. Comparisons with observational data reveal that ROMS reproduces a realistic mean state of the SCB oceanic

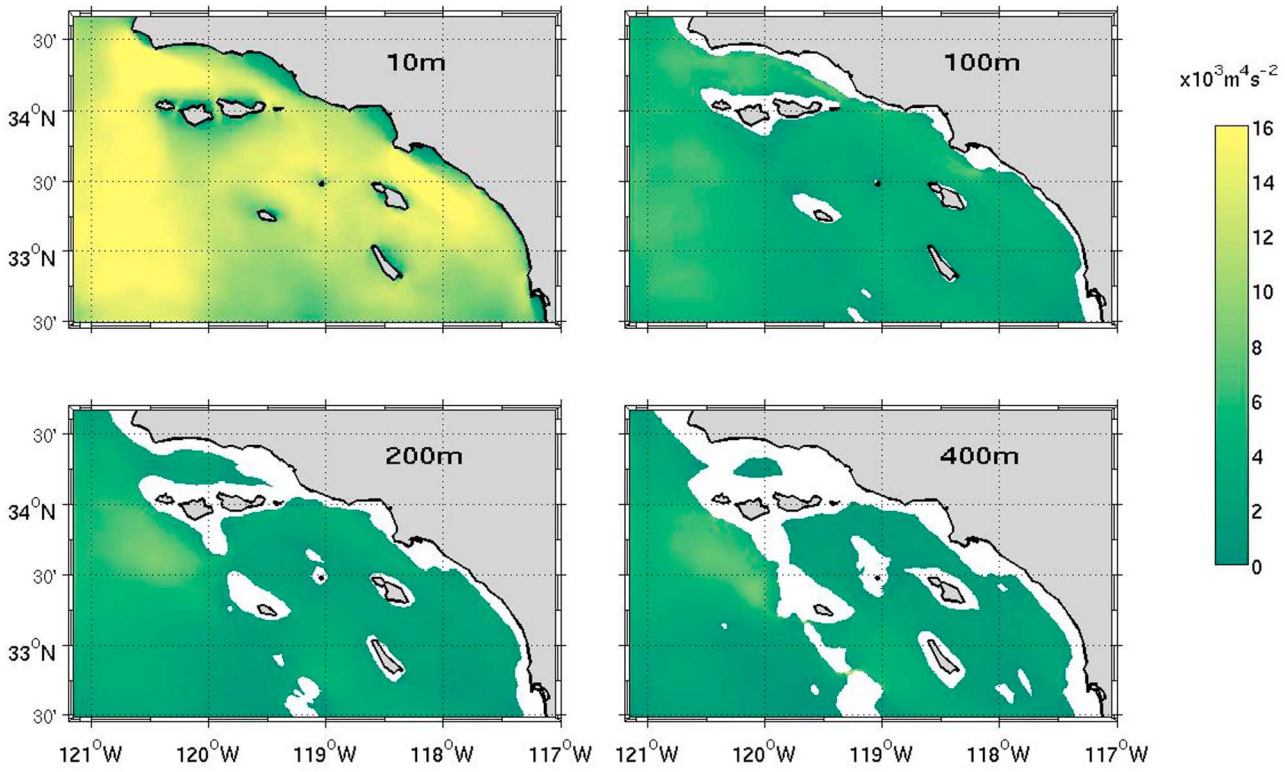

Figure 2. The mean eddy kinetic energy (EKE) at four levels (10 m, 100 m, 200 m, and 400 m). The mean EKE is averaged over the 12 years from 1996 to 2007. The EKE is calculated from high-passed (90 days) velocity fields (unit, 10^3 m^4 s^{-2}).

circulation, as well as its inter-annual (mainly as a local manifestation of an ENSO event), seasonal, and intraseasonal (eddy-scale) variations. The simulation also exhibits three subdomain-scale, persistent (i.e., standing), cyclonic eddies related to the local topography and wind-forcing: the Santa Barbara Channel Eddy, the Central-SCB Eddy, and the Catalina-Clemente Eddy. We find high correlations of the wind stress curl with both the alongshore pressure gradient and the eddy kinetic energy level in their variations on seasonal and longer time scales. The model exhibits intrinsic eddy variability with strong topographically related heterogeneity.

[8] The high-resolution numerical product has been used by the oceanographic community. Besides it was used for the study of island wakes [*Dong and McWilliams*, 2007] and upwelling events [*Dong et al.*, 2011], it was applied to studies of Lagrangian assessment of surface current dispersion in the coastal ocean [*Ohlmann and Mitarai*, 2010], for quantifying connectivity [*Mitarai et al.*, 2009] and for potential larval connectivity in the SCB [*Watson et al.*, 2010, 2011]. The model configuration is also applied to a real time forecast for the oceanic circulation in the SCB, see its website: ourocean.jpl.nasa.gov/SCB.

[9] In summary, the high-resolution (1 km) numerical product used for the present study has been validated. It is sampled as daily averages with a 1-km horizontal resolution and 40 vertical levels with an s-coordinate system. Specially for this present study, velocity fields are linearly interpolated onto 9 vertical levels: 10 m, 50 m, and then all the way to 400 m with a uniform interval of 50 m (due to the surface-intensified setting of the model configuration, the vertical resolution might not be enough to resolve the variation beyond 400 m).

2.2. General Analysis of Eddy Variation

[10] Prior to the identification of individual eddies using eddy detection schemes, we use a general way to examine eddy variations by extracting high-pass (90 days) velocity fields. The 90-days high-pass scale is the intraseasonal-scale variation, which is considered as an eddy scale. The kinetic energy calculated from the high-pass velocity data is defined to be the eddy kinetic energy (EKE). Its distributions at four levels (10 m, 100 m, 200 m and 400 m) are plotted on Figure 2. The mean EKE at the surface is the largest in the western portion of the Santa Barbara Channel, within the channel between the Palos Verdes Peninsula and Catalina Island, and around the headlands; around islands and near the shoreline, however, the EKE is relatively low. Similar mean EKE patterns at the surface using eight-year (1996–2003) data are given by *Dong et al.* [2009a]. The pattern extends to 100 m. On the levels of 200 m and 400 m, the higher EKE locations are immediately south of the western entrance of the Santa Barbara Channel and near the edge of the shelf. The EKE distribution suggests that it is related to the topography in the SCB. Figure 2 also shows the magnitudes of the EKE decrease sharply away from the surface. The vertical profile of the mean EKE averaged over the area of water at each level is plotted in Figure 3. From the surface to 50 m (nominally the bottom of the Ekman layer), the EKE drops by 1/3, to 100 m (in the middle of the thermocline) by 2/3. Below the thermocline (150 m), the EKE remains

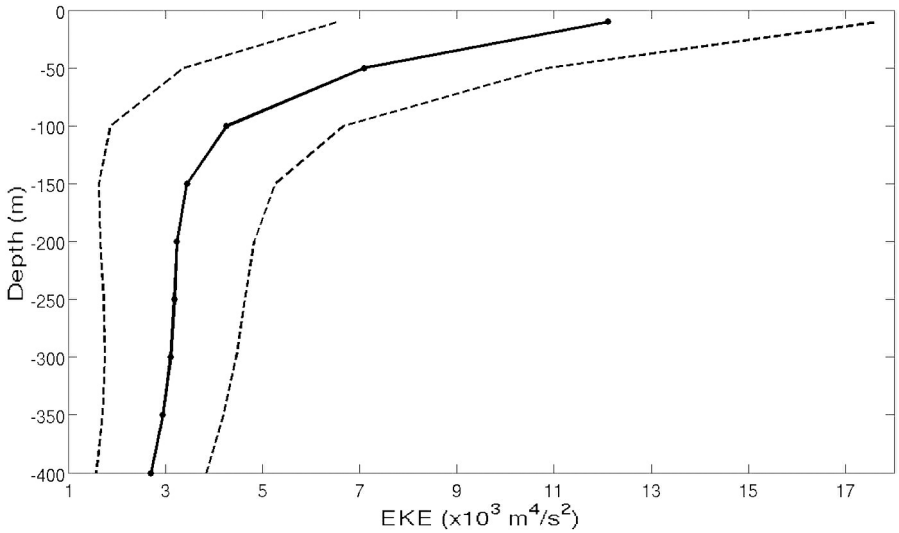

Figure 3. A vertical profile of the mean EKE averaged over the area of water points at each level. The solid line is the mean EKE, and dashed line is its standard deviation.

almost constant with a smaller range in the variation. Temporal variation in the surface EKE has been extensively discussed by *Dong et al.* [2009a], and much weaker temporal variations are evident in deep levels (not shown).

3. Eddy Identification Schemes

3.1. Velocity Geometry Eddy Detection Schemes

[11] The automatic eddy detection algorithm for the high-resolution numerical product was developed by *Nencioli et al.* [2010]. It has been applied to eddy detection in Hawaiian Islands wake by *Dong et al.* [2009b]. It has also been applied to eddy detection in altimetry-observed sea surface height anomaly data (Y. Liu et al., Eddy analysis in the subtropical zonal band of the North Pacific Ocean, submitted to *Deep-Sea Research*, 2011) and sea surface temperature-derived thermal velocity field [*Dong et al.*, 2011]. The method is based on some of the features that characterize the velocity field associated with mesoscale eddies [e.g., *Dickey et al.*, 2008], such as minimum velocities in the proximity of the eddy center, and tangential velocities that increase approximately linearly with distance from the center before reaching a maximum value and then decaying.

[12] Four constraints are defined based on the characteristics of eddy velocity fields:

[13] 1. Along east-west section, meridional velocity, U_y, has to reverse in sign across the eddy center, and its magnitude has to increase away from it.

[14] 2. Along north-south section, zonal velocity, U_x, has to reverse in sign across the eddy center, and its magnitude has to increase away from it; the sense of rotation has to be the same as for it.

[15] 3. The velocity magnitude has a local minimum at the eddy center.

[16] 4. Around the eddy center, the directions of the velocity vectors have to change with a constant sense of rotation, and the directions of two neighboring the velocity vectors have to lie within the same, or two adjacent quadrants (the four quadrants are defined by the north-south and west-east axes: the first quadrant encompasses all the directions from east to north; the second quadrant the directions from north to west; the third quadrant the directions from west to south; and the fourth quadrant the directions from south to east).

[17] These constraints are applied to each point of the velocity field anomaly fields with the respect to the 12-year time mean. The points for which all four conditions are satisfied are defined as eddy centers. In addition, eddy boundaries and moving tracks are also identified (see *Nencioli et al.* [2010] for the details).

3.2. An Approach to Detecting Vertical Structure of an Eddy

[18] Using the spatial and temporal information for eddies at nine individual vertical levels using the algorithm described in section 3.1, we trace eddies downward from the surface to deep layers and then construct their 3-D structures. One can directly extract the whole 3-D data from the numerical product, however, given the complexity in the bottom topography, quantifying an eddy's statistical characteristics requires repeated local linear projections and eddy detection procedures to determine the eddy statistical quantities. Here, we introduce a method to extract a 3-D structure of an eddy using existing eddy data sets for the 9 individual levels. It is assumed that an eddy center does not drift by 1/4 of its radius when it goes down 50 m if the eddy penetrates 50 m deeper. The procedure follows:

[19] 1. With the information for an eddy at the surface (10 m) obtained by using the above eddy detection scheme: eddy center (X_1, Y_1), occurrence time (T), eddy radius (R_1) and polarity, we check if there is an eddy with the same polarity at the same occurrence time at an immediately lower level (50 m below the current level) whose center is located within a circular area around the eddy center: the circle's center is $P_1(X_1, Y_1)$ and radius is $0.25R_1$.

[20] 2. If such an eddy is not found at the level of 50 m, the eddy's maximum depth is determined to be shallower than 50 m. If such an eddy is found, then the center $P_2(X_2, Y_2)$,

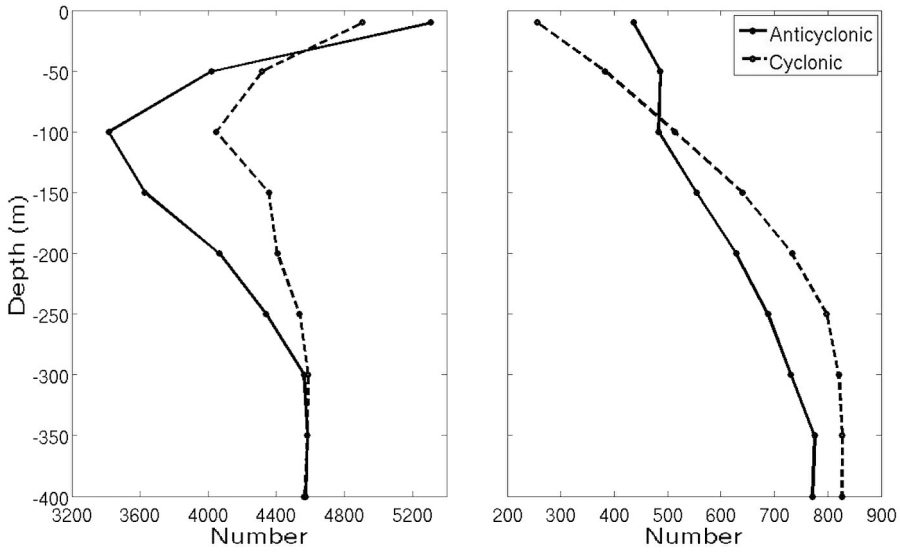

Figure 4. Vertical profiles of the number of eddies generated. (left) Number of eddies with lifetime equal to or longer than 3 days. (right) Number of eddies with lifetime equal to or longer than 20 days.

radius (R_2), and other parameters of the eddy at the level of 50 m are recorded.

[21] 3. Using the eddy center, radius, occurrence time and polarity, we check if there is an eddy with the same polarity and occurrence time at an immediately lower level (100 m) whose center is located within a circular area around the center: the circle's center is $P_2(X_2, Y_2)$ and radius is $R_2/4$.

[22] 4. Then, we repeat the above procedures until we reach the level of 400 m. Then the quantitative features of the eddy can be obtained: centers (P1, P2, …, P9), radius (R1, R2, … R9), and other parameters.

[23] By these procedures a discrete 3-D eddy data set with a vertical resolution of 50 m. Of course, if more vertical levels are extracted, the vertical structure can have a higher resolution.

4. Eddy Statistical Characteristics

4.1. Eddy Number and Lifetime

[24] With the application of the above automated velocity geometry eddy detection to the velocity anomaly fields at the 9 levels, which was introduced in section 2, we develop a 3-dimensional eddy data set in the SCB. It includes eddy location, time, polarity, and boundary at each level. Other eddy parameters, such as relative vorticity, size and lifetime, are also derived. In total, 57062 cyclonic and 46874 anticyclonic eddies are detected at the surface and 61476 cyclonic and 64873 anticyclonic eddies are found at the level of 400 m. The total numbers include repetitive counting of the same eddies through their lifetimes. If we count eddies at each time step of its lifetime as one occurrence, the total numbers of individual eddies are 12240 cyclonic and 12510 anticyclonic eddies at the surface, and 8099 cyclonic and 8049 anticyclonic eddies at the level of 400 m. Considering some uncertainties associated with the eddy detection scheme and sporadic noises in the numerical data, in the following analysis, we only count eddies whose lifetimes are equal to or longer than 3 days. Then there are 5308 cyclonic and 4906 anticyclonic eddies at the surface, and 4573 cyclonic and 4564 anticyclonic eddies at 400 m. There are about 8.0% more cyclonic than anticyclonic eddies at the surface but almost the same number for anticyclonic and cyclonic eddies at 400 m. The greater number of cyclonic eddies at the surface might be due to the prevailing positive wind curl in the area.

[25] The variation of eddy numbers from the surface to 400 m is shown in Figure 4. It indicates that the eddy number does not monotonically decrease or increase but rather has minimum number at 100–200 m where the density stratification is located. Since eddies in their lifetime are counted as one eddy, the eddy number can be used as the eddy generation number. It shows that fewer eddies are generated within the stratification layer than at the surface and even below the stratification. It implies some eddies generated either at the surface or at deep levels cannot penetrate the stratification layer. It should be noted that the vertical profile of the eddy number changes with the criteria of the life time chosen. For example, for eddies whose lifetimes are equal to or longer than 20 days, there are more eddies in deeper ocean, i.e., the eddies generated in the deeper ocean tend to live longer. An eddy's lifetime is defined by the interval between the first and last times when the eddy is detected. To exclude eddies which are advected out of and into the domain, in other words, they are not generated or terminate locally, we do not count eddies first and last found 10 grid points next to the three open boundaries, which is about the length of the mean advection scale for one day (assuming the mean velocity is about 0.1 m/s).

[26] The eddy lifetime variation with the depth is directly confirmed by a figure showing vertical profile of eddy lifetimes in Figure 5. It shows that anticyclonic eddies in the deep ocean live longer than those near the sea surface, but cyclonic eddies display the less difference between the surface and the deep water. This can be explained with the fact that the SCB is located in a positive wind curl area, which favor cyclonic eddies at the surface. To further examine the eddy lifetimes, Figure 6 shows the histogram of eddy lifetimes at four levels. The numbers of both anticyclonic and cyclonic eddies are approximately symmetric in terms of the

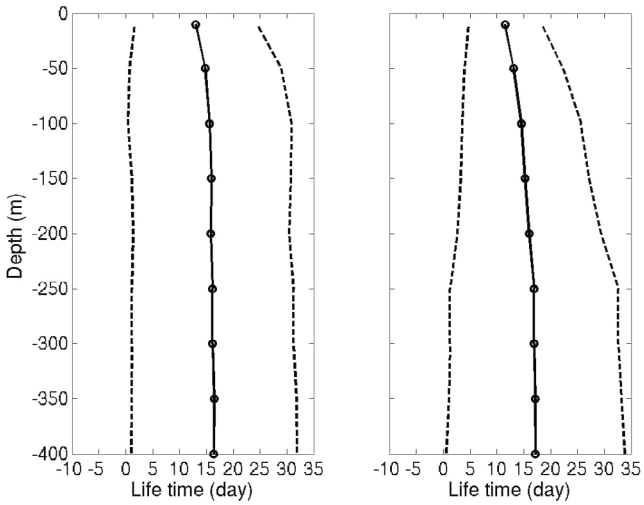

Figure 5. Vertical profile of eddy lifetime. The solid lines are mean lifetime, and dashed lines are from the subtraction/addition of standard deviation from/to the mean values, representing the variation ranges.

lifetimes. Some eddies can survive for a few months (which are not shown). Compared with results for open oceans [e.g., *Chelton et al.*, 2011; Liu et al., submitted manuscript, 2011], eddies in the SCB have relatively shorter lifetimes, which might be due to stronger advection in the coastal ocean and greater sinking source (friction) along the horizontal and in the bottom boundaries in the coastal ocean.

4.2. Eddy Sizes

[27] Histograms of eddy sizes at four levels are shown in Figure 7. The size of an eddy is defined as its radius. Cyclonic and anticyclonic eddies are more symmetric at lower levels than at the surface in terms of eddy size: at the surface there are more cyclonic eddies, which might be due to favorable positive wind curl at the surface as argued above. The peak number is located at about 5 km, which is considered as the scale of submesoscale eddies given that the mean deformation radius is about 20–30 km [*Dong and McWilliams*, 2007]. It is consistent with what *DiGiacomo and Holt* [2001] found using SAR imageries that they collected: most eddies' sizes are smaller than 10 km. Spatial distributions of eddy sizes at four levels are plotted in Figure 8. Eddies to the west of Santa Rosa Ridge (see Figure 1 for the map) and the western part of the SCB are much larger than those in the rest of the domain. Eddies between San Clemente Island and the coast, San Nicholas Island and San Clemente Island are also large. Eddy sizes decrease with the depth, which is further confirmed by the vertical profiles of both cyclonic and anticyclonic eddies as indicated in Figure 9. Mean eddy sizes are about 8–10 km at the nine levels with a variation range of 3 km $\sim$ 16 km.

4.3. Eddy Vorticity

[28] Theoretically, relative vorticity magnitude within an eddy decreases from its center to its boundary (reaches zero). The boundary of an eddy defined in the eddy detection scheme comprises turning points where the velocity magnitude starts to decrease from its increasing trend, i.e., the relative vorticity is equal to zero. The relative vorticity of an eddy is defined as the mean value within the eddy area confined by its boundary. Histograms of eddy relative vorticity normalized by the planetary rotation at four levels are shown in Figure 10, which normalized relative vorticity asymmetry in cyclonic and anticyclonic eddies near the sea surface, and the relative vorticity of cyclonic eddies has wider variation in their Gaussian distribution. The normalized relative vorticity with the peak number is about 0.3. The spatial distributions of normalized relative vorticity at four levels (10 m, 100 m, 200 m and 400 m) averaged over 1/16 degree $\times$ 1/16 degree bins, are plotted in Figure 11,

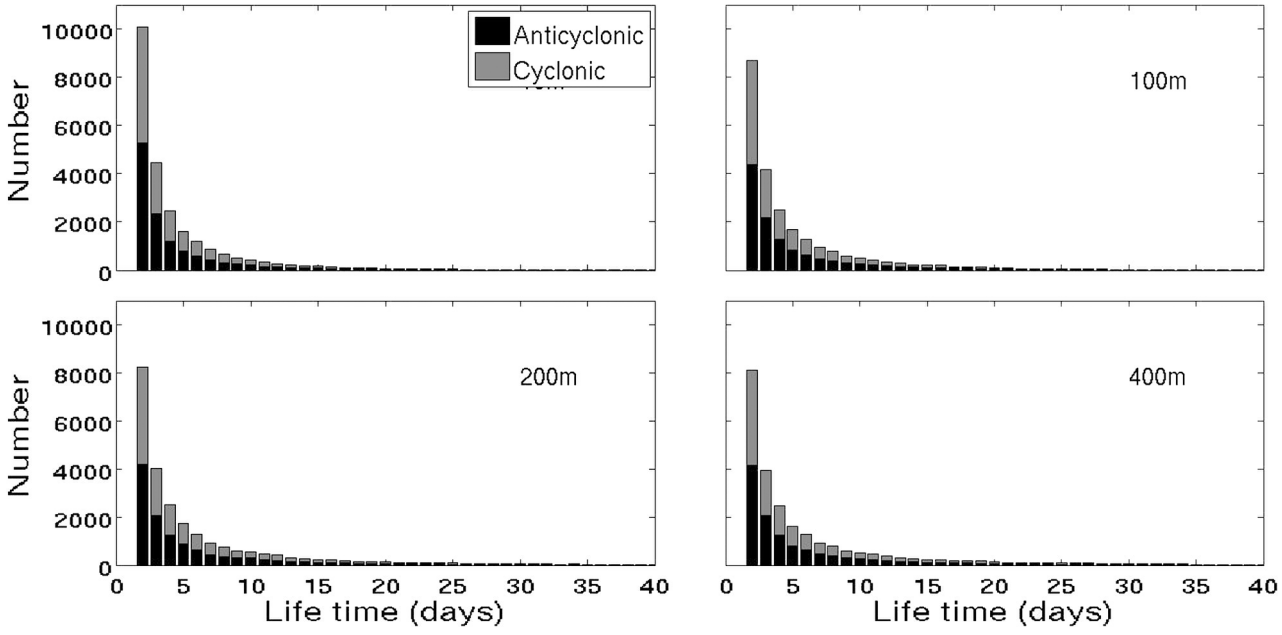

Figure 6. Histograms of eddy lifetime at four levels.

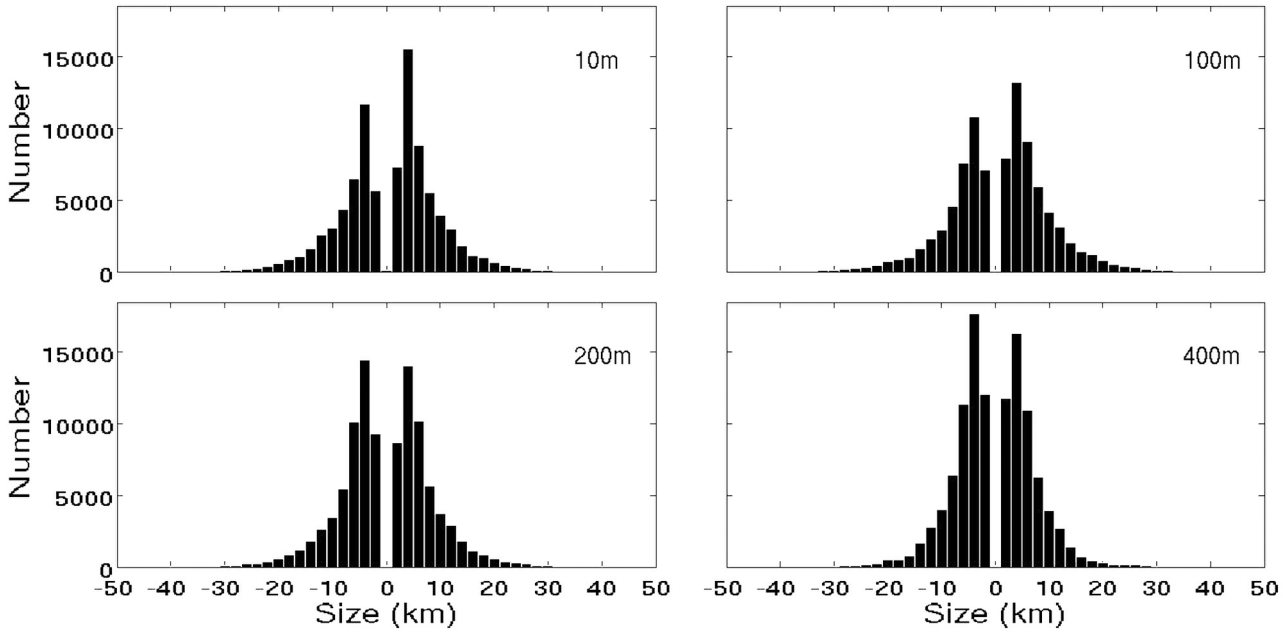

Figure 7. Histograms of eddy sizes for four levels (10 m, 100 m, 200 m, and 400 m). Positive (negative) eddy sizes denote cyclonic (anticyclonic) eddies.

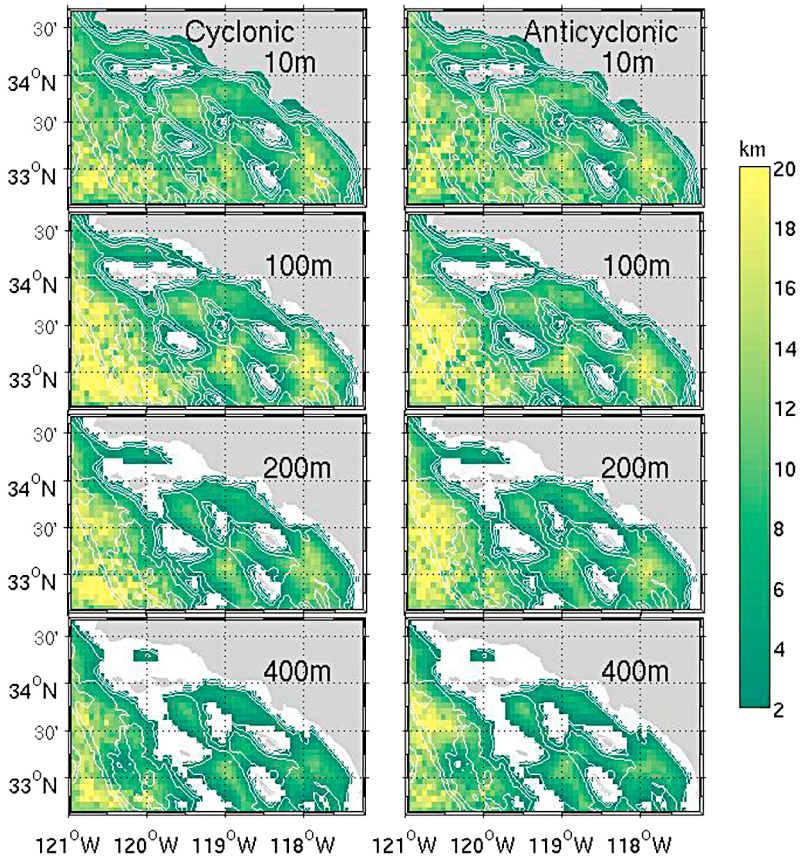

Figure 8. Eddy size distributions at four levels (10 m, 100 m, 200 m, and 400 m): (left) cyclonic eddies and (right) anticyclonic eddies (unit, km).

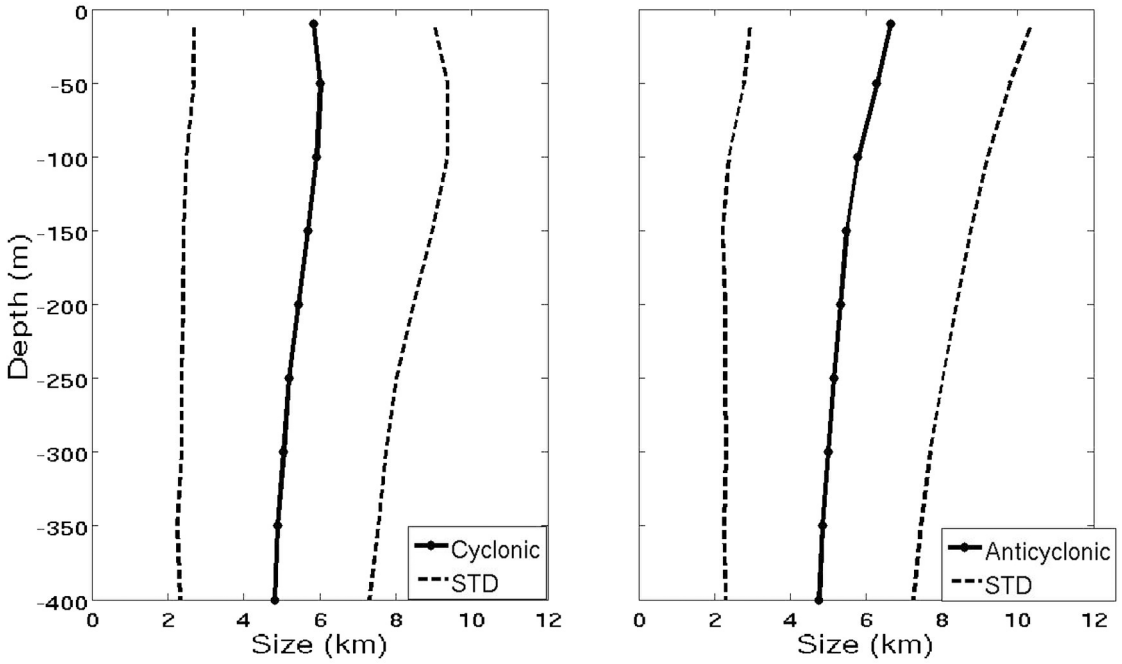

Figure 9. The same as Figure 5 except for eddy sizes.

which shows larger values around islands and headlands. Both eddy relative vorticity and EKE are used to present eddy intensity, however they might give different information of eddies: EKE is related to eddy velocity magnitude and relative vorticity is related to the velocity gradient. Around islands, due to the geostrophic constrain, the surrounding shelves constrain the current from flowing too close to the islands and weaken the flow, but the velocity gradient might not be weaker. Another reason for the discrepancy between the EKE and the mean relative vorticity distributions is because the vorticity plotted in Figure 11 is the mean over identified eddies, most of which are generated around islands (section 6.1) and their sizes are relatively smaller (Figure 8) with relatively higher magnitudes of relative vorticity (section 6.2). Figure 11 also shows that cyclonic eddies have much stronger relative vorticity than anticyclonic eddies at the surface, and the magnitude decreases sharply from the surface to the deep ocean for cyclonic eddies but not for anticyclonic eddies. This demonstrates that again the upper part of the ocean is

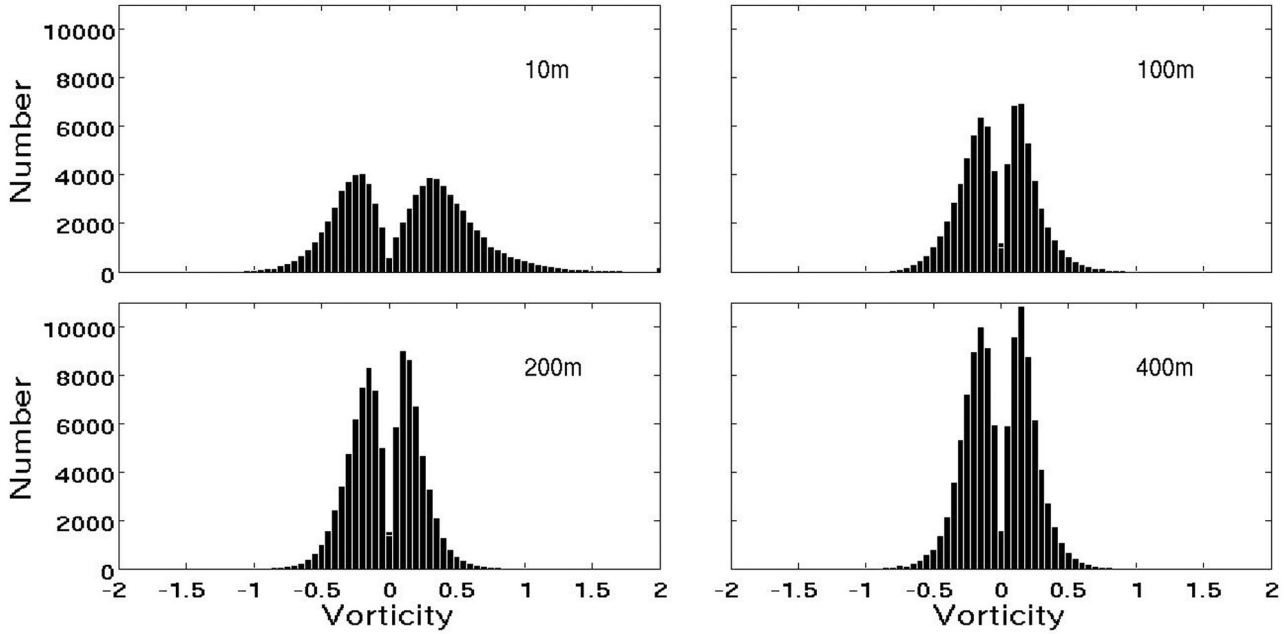

Figure 10. The same as Figure 7 except for eddy relative vorticity normalized by the background planet vorticity.

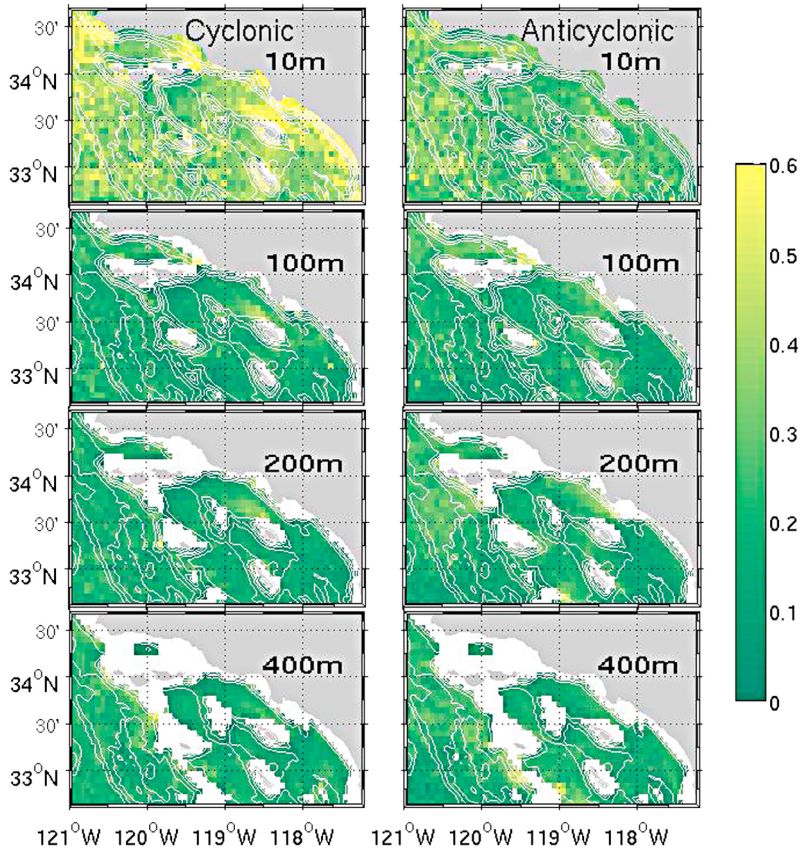

Figure 11. Same as Figure 8 except for the relative vorticity absolute values.

affected by positive wind curl more than at lower levels. This is to be expected. The vertical profile of mean normalized relative vorticity in Figure 12 shows that the relative vorticity decreases with depth.

4.4. Eddy Evolution

[29] An eddy is well characterized by eddy parameters, such as, eddy radius, relative vorticity, kinetic energy and deformation rate. The former two parameters have been discussed in the preceding sections. The eddy kinetic energy defined here is the kinetic energy averaged within an eddy area (from the eddy center to its boundary). The eddy deformation rate is defined as $(\gamma_1^2 + \gamma_2^2)^{1/2}$, where $\gamma_1 = (\partial v/\partial x) + (\partial u/\partial x)$ and $\gamma_2 = (\partial u/\partial x) - (\partial v/\partial y)$ are the shear deformation rate and the stretching deformation rate [*Carton*, 2001; *Hwang et al.*, 2004; Liu et al., submitted manuscript, 2011]. The temporal

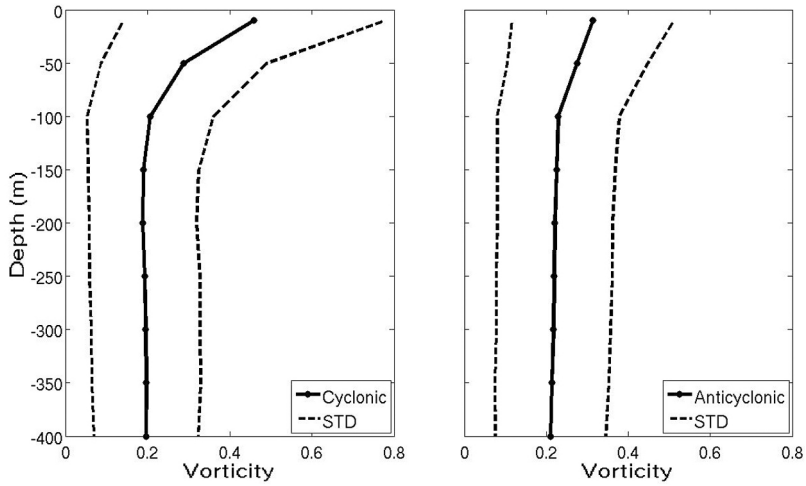

Figure 12. Same as Figure 9 except for relative vorticity absolute values.

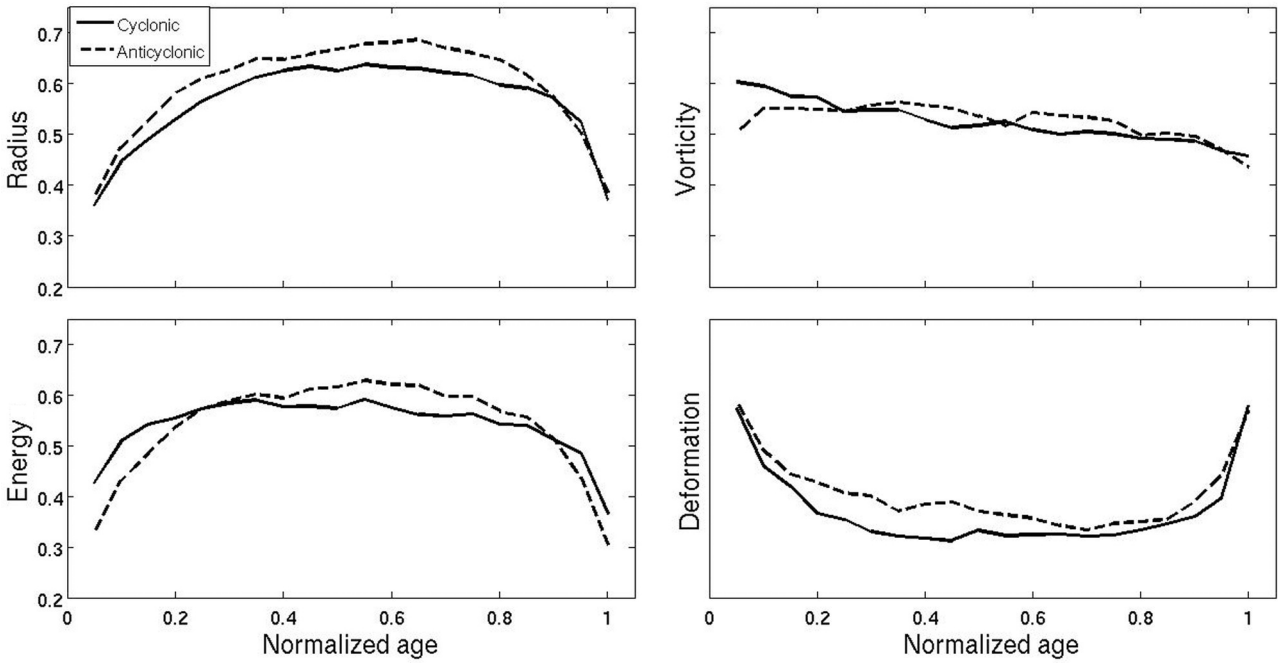

Figure 13. The time evolution of mean eddy characteristic parameters: (top left) radius, (top right) relative vorticity, (bottom left) kinetic energy, and (bottom right) deformation. Each eddy's age is normalized by its life span. Each parameter of each eddy is normalized by its maximum magnitude of the parameter, and the mean eddy parameters obtained by averaging over eddies with life span longer than 20 days are plotted in the figure. Dashed and solid lines denote cyclonic and anticyclonic eddies, respectively.

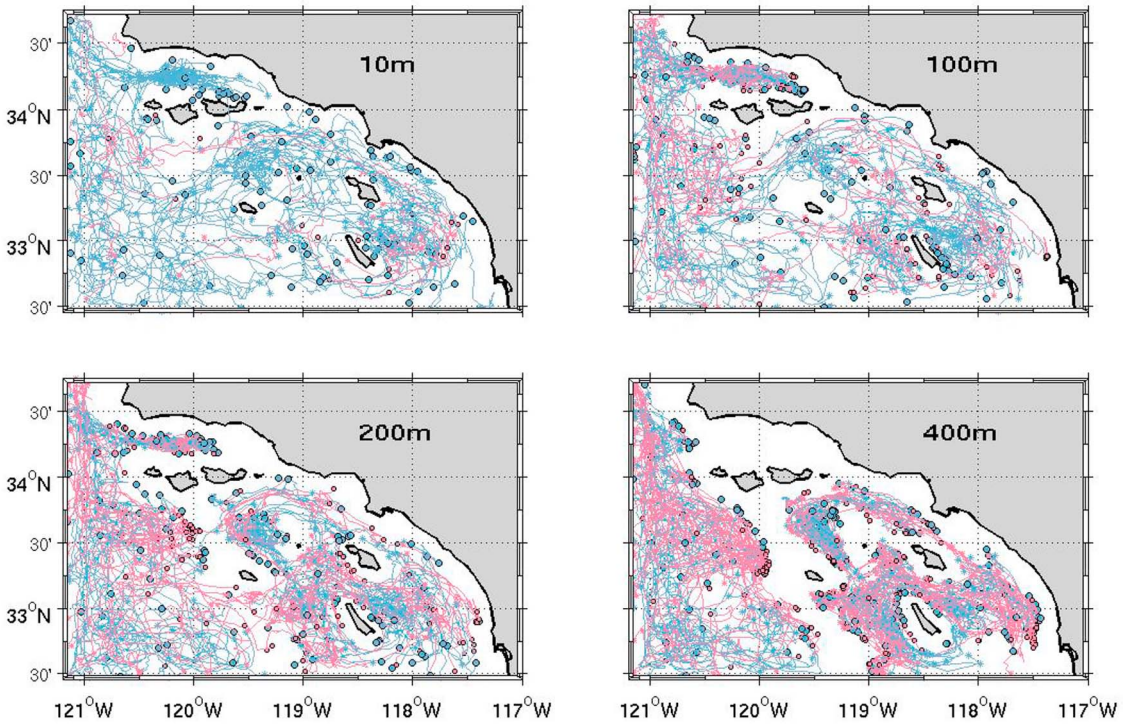

Figure 14. Trajectories of eddies which live longer than 50 days. Cyclonic and anticyclonic eddies are plotted in light blue and light red, respectively.

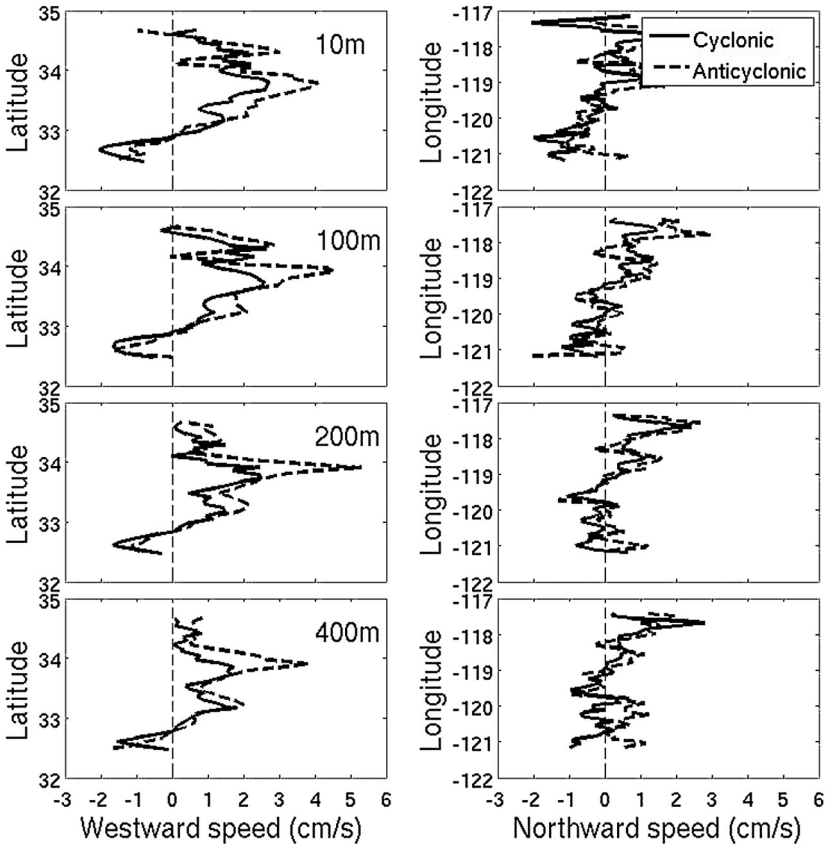

Figure 15. Eddy (left) westward and (right) northward moving speeds vary with latitude (averaged every 0.25 degree in latitude band) at four levels: 10 m, 100 m, 200 m, and 400 m.

evolutions of these parameters during the lifetime of each eddy well present how an eddy evolves. Following a method proposed by Liu et al. (submitted manuscript, 2011), we consider eddies with long lifetimes equal to or longer than 20 days. With this definition, the total numbers of such eddies are: 436 cyclonic eddies and 256 anticyclonic eddies at the surface. An eddy age is normalized by its lifespan and parameters are normalized by the corresponding maximum in the lifespan of each eddy and by taking average over all eddies with life spans longer than 20 days. Normalized temporal evolutions for these four parameters are thus obtained and plotted in Figure 13. Eddy size and kinetic energy increase during the first 1/5 of an eddy's life cycle (youth) and then it remains stay stable for next 3/5 of its life cycle (adult). In the last 1/5 of the mean life cycle (aged), these parameters decrease sharply. The deformation rate shows the opposite trend, in its first 1/6 of life cycle (youth), the rate decreases and then stays roughly constant for the next 2/3 of the life cycle and finally it increases sharply before the eddy eventually dies. The lifetime eddy evolution for lower levels is similar to that at the surface (not shown).

4.5. Eddy Movement

[30] Shown in Figure 14 are plots of trajectories of cyclonic and anticyclonic eddies which live longer than 50 days at four levels (10 m, 100 m, 200 m and 400 m). Generally, these eddies move westward in the northern part of the SCB and return eastward in the southern part via an offshore path turning southward. When averaged over zonal bands of 1/4 degree in width, shown in Figure 15 (left), the westward velocity of eddies varies with the latitude: north of about 33°N, eddies move westward and the peak of the speed is reached at 34°N; south of 33°N, eddies move eastward. The zonal movement is due to the combination of β effect and self-advection [*McWilliams and Flierl*, 1979]. Shown in Figure 15 (right), the mean meridional velocity of eddies at all levels averaged over meridional bands of 1/4 degree in width is northward east of 119°W and southward west of 119°. As discussed in section 1, the mean circulation in the SCB is a cyclonic gyre, which contributes to the pattern of eddy movement.

4.6. Eddy Vertical Structure

[31] In sections 4.1–4.5, it is clearly shown that eddies vary with depth in terms of eddy parameters. In this section, we apply the approach introduced in section 3.2 to examine three-dimensional structures of eddies. Starting from the sea surface by looking downward, we try to determine how deep each eddy can penetrate, i.e., the depth of the eddy bottom. The histogram of eddy depth (limited to 400 m) is plotted in Figure 16. The number at each level in Figure 16 is the number of eddies only found at one level and levels shallower (deeper) by looking upwards (downward). Most eddies can reach less than 50 m. The number of eddies

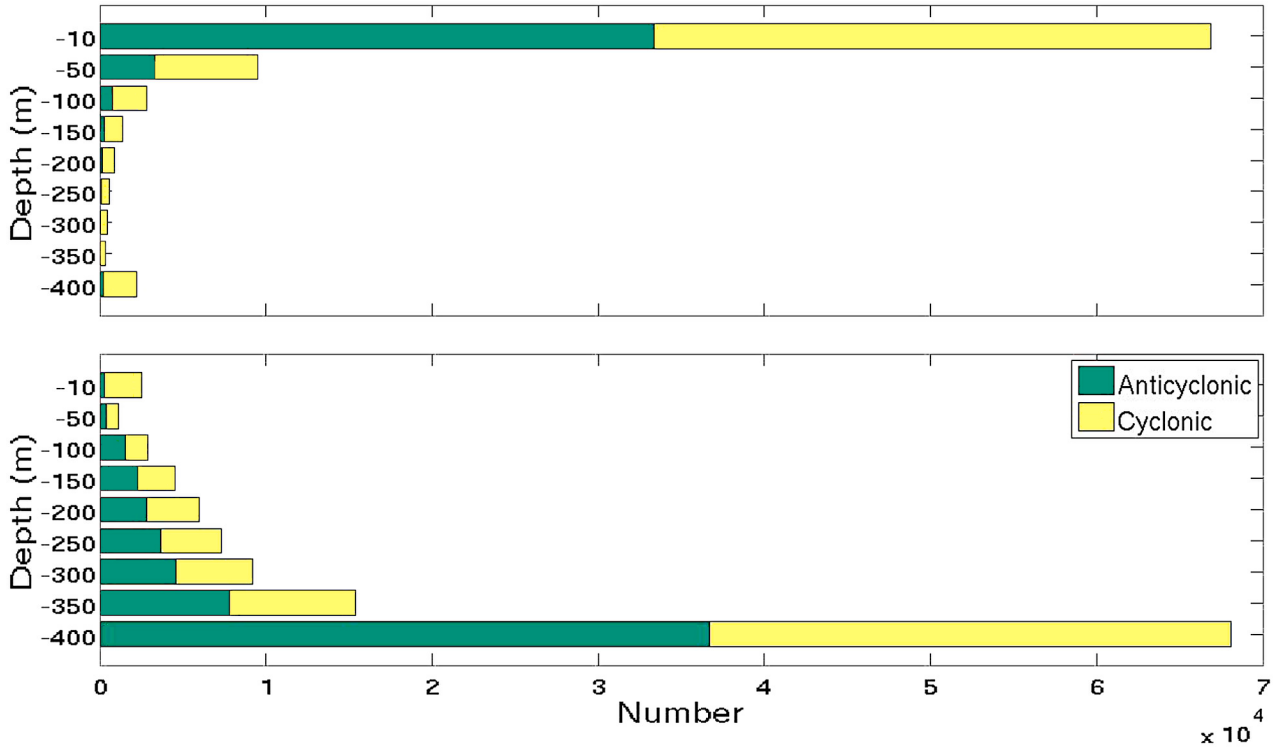

Figure 16. (top) Histogram of numbers of eddies at one level which can be detected at that and all the shallower levels but not deeper levels by looking downward from the surface (a level of 400 m). (bottom) Histogram of numbers of eddies at one level which can be detected at that and all the deeper levels but not shallower levels by looking upward from the surface (a level of 400 m).

which can reach deeper than 50 m decreases dramatically. This figure also shows that cyclonic eddies can reach deeper than anticyclonic eddies. When looking upwards from the level of 400 m, the similar trend is seen: most eddies cannot penetrate to the surface.

[32] In total, there are about 2700 eddies which can penetrate to 400 m as listed in Table 1. Due to some uncertainty in the criteria of eddy drifting distance, there are slight differences in upward- and downward-looking penetrating eddy numbers. From the 400 m-penetrated eddy data, it is found that there are three types of eddies in terms of size with respect to vertical variation (see Figure 17): (1) bowl-shaped: an eddy has the largest size at the surface; (2) cone-shaped: an eddy has the largest size at the bottom (400 m); (3) lens-shaped: an eddy has the largest size in the stratification layer. Table 1 shows the numbers of three types of eddies. Most eddies (65%) are bowled-shaped and 20% are lens-shaped and about 15% are cone-shaped. It is also interesting to be noted that 90% of 400-m penetrated eddies are cyclonic eddies, which is consistent with Figure 16.

5. Eddy Variation in the SBC during September

[33] The upwelling and downwelling associated with eddies can make significant impacts on the fine particle suspensions and chemical and biological processes in the upper ocean, which can affect the penetrating depth of visible sunlight (T. Dickey et al., submitted manuscript, 2011). Thus eddy analysis can help us better understand the data collected in the RyDyo experiment.

[34] The RaDyO experiment was conducted in the SBC in September 2008. Though the current numerical product has not yet been extended to the year of 2008. However, with the availability of external forcing information, the decade-long numerical solution does allow us to examine the eddy variation in the season of the SBC RaDyO experiment.

Table 1. Numbers of Three Types of Eddies Penetrating Through 400 m

	Bowl-Shaped			Lens-Shaped			Cone-Shaped			
	Cyclonic	Anticyclonic	Total	Cyclonic	Anticyclonic	Total	Cyclonic	Anticyclonic	Total	Total
Downward	1556	189	1745	491	67	558	367	17	384	2687
Upward	1442	185	1627	545	92	637	415	25	440	2704

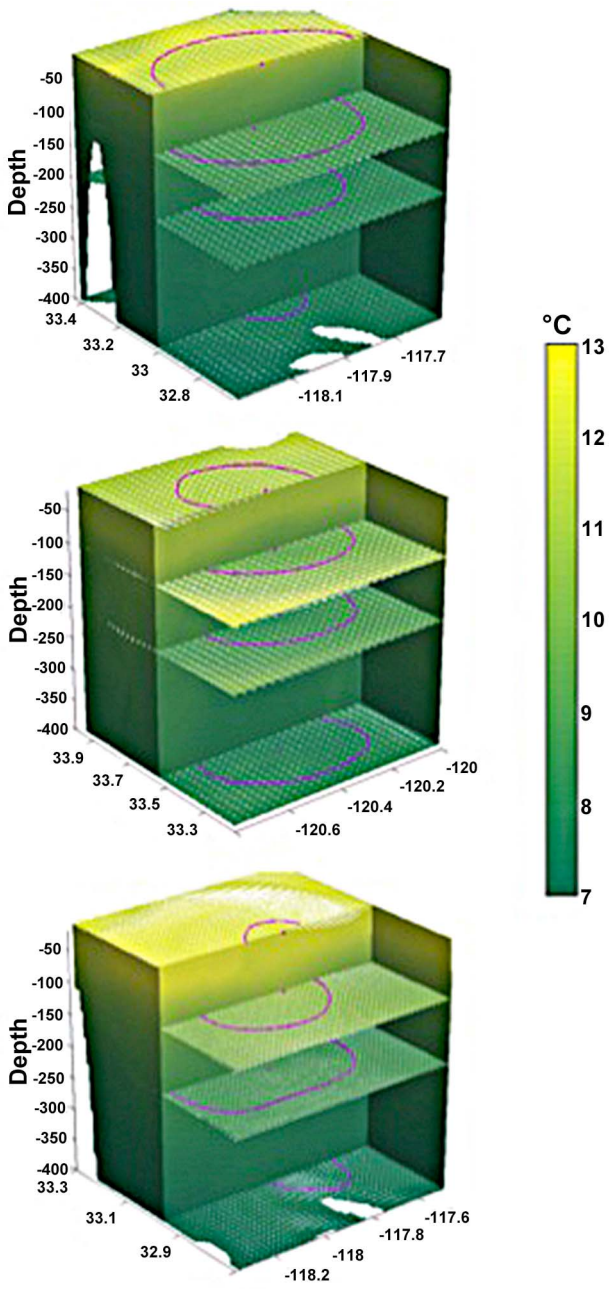

Figure 17. Examples for three types of eddies in term of their vertical structure: (top) bowl-shaped, (middle) cone-shaped, and (bottom) lens-shaped. White vectors are velocity (unit, m/s), and contours are eddy boundaries.

[35] Figure 18 shows that the SBC is one of the important sites for the generation of both cyclonic and anticyclonic eddies, especially at the eastern entrance to the Channel. Also, a persistent cyclonic eddy has been frequently observed in the western portion of the basin. In *Dong et al.* [2009a, Figure 7], in situ, drifter-derived velocity and numerical modeling data all confirm the year-around existence of this SBC-size cyclonic eddy. Figure 19 shows that the eddy generation rate in September is one of the highest for any month in a given year for both cyclonic and anticyclonic eddies. The presence of eddies in the SBC during the RaDyO experiment period likely influences the temporal and spatial variations of optical properties and light penetration, which has been reported in other articles in this issue.

6. Discussion and Summary

6.1. Eddy Generation and Termination

[36] To identify where and when eddies are generated and terminated can help to better understanding of the mechanisms for eddy generation and termination inside the domain. The first (last) record in the time series of each eddy lifetime is defined as the time and location of eddy generation (termination). As discussed in section 4.1, eddies, which move into (out of) the domain are not considered to be generated (terminated) locally. To exclude those eddies technically, we remove the first (last) records that are found within 10-grid strips along three open boundaries from the generation (termination) records.

[37] The spatial distributions of eddy generation number at four levels are plotted in Figure 18. From the surface to 400 m, most of eddy generation sites are located either around islands or near the headlands along the coastline. The distribution pattern strongly suggests that the islands and headlands play primary roles in eddy generation [*Dong and McWilliams*, 2007].

[38] Seasonal and interannual variations for eddy generation at 9 levels are plotted in Figure 19. At the surface, the cyclonic eddy generation does not show a strong seasonal variation, but during fall, anticyclonic eddies have the highest number. This is because the SCB is in an area with the strong positive wind stress curl and the positive wind stress curl is the weakest in the fall [*Dong et al.*, 2009a] which favors the generation of anticyclonic eddies. In the subsurface, the sandwiched structure shows that fewer eddies are generated in the stratified layer around years. The magnitude of the seasonal variation for cyclonic eddy generation is smaller than that for anticyclonic eddies. For the interannual variation, the eddy generation in 2001–2002 has the minimum number, which could be caused by the interannual variation in the wind curl at the sea surface [*Dong et al.*, 2009a].

[39] Figure 20 shows the spatial distributions of eddy termination for four levels. The eddy termination areas spread much wider from their generation regions. There are similar seasonal and interannual variations in eddy termination (not shown) as that for eddy generation because most eddy lifetimes in the SCB are less than one month.

6.2. Eddy Dynamical Balance

[40] There are two types of eddies in terms of dynamic balance: the one is geostrophic- balanced eddy and the other is ageostrophic-balanced eddy. The following equation can be used to determine if an eddy is in a geostrophic balance:

$$\frac{1}{\rho_0}\frac{\partial P}{\partial r} + fU_\theta + \left(-U_r\frac{\partial U_r}{\partial r} - \frac{U_\theta}{r}\frac{\partial U_r}{\partial \theta} + \frac{U_\theta^2}{r}\right) = 0 \qquad (1)$$

where ρ_0 is the reference density, P is the pressure, r is the radial distance from the center of the eddy, U_r and U_θ are the

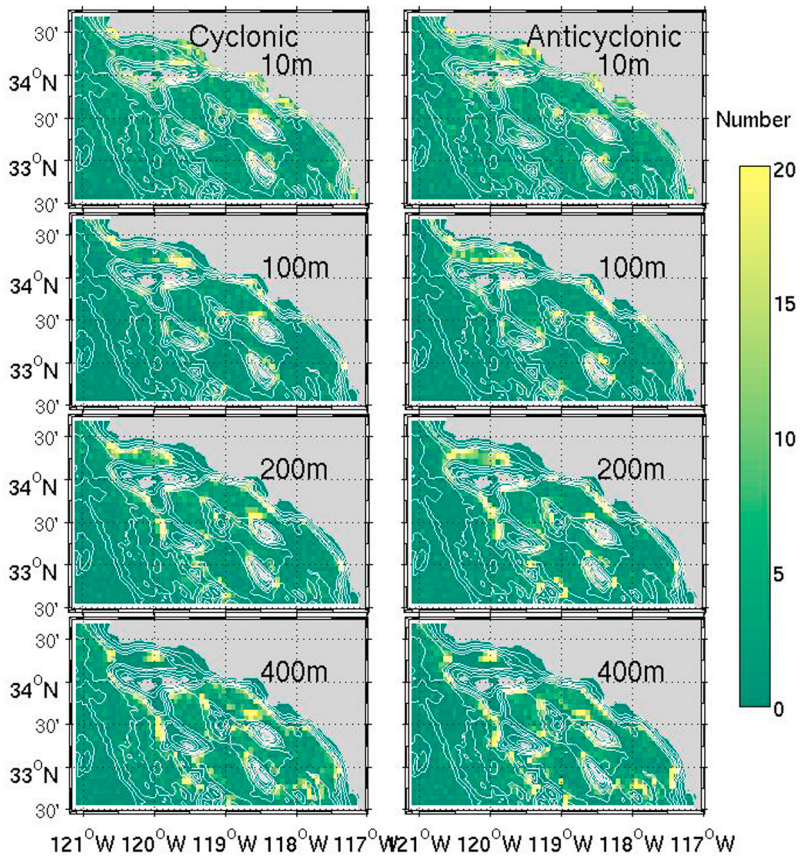

Figure 18. Eddy generation number distribution inside the domain at four levels (10 m, 100 m, 200 m, and 400 m). (left) Cyclonic eddies (right) Anticyclonic eddies. White contours are bathymetries.

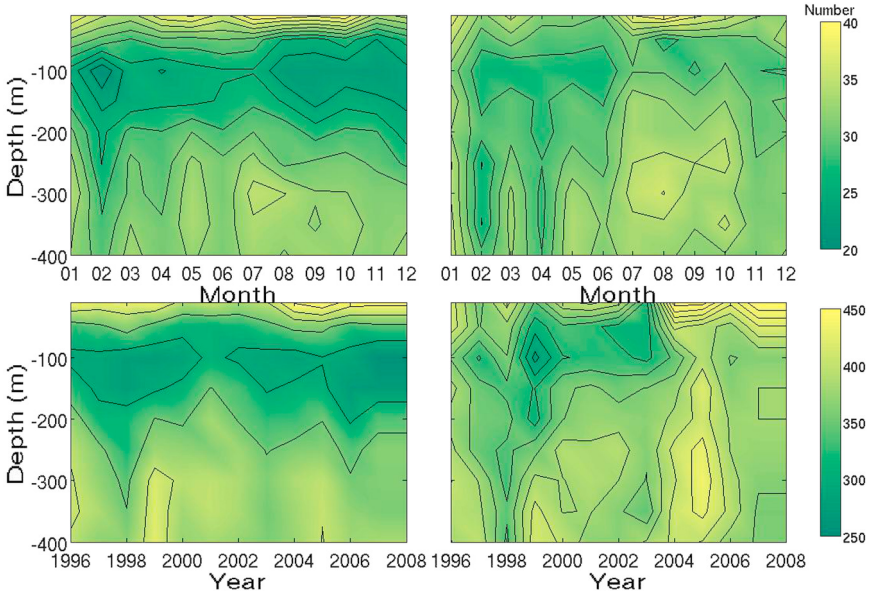

Figure 19. (top) Seasonal and (bottom) interannual variation in eddy generation inside the domain: (left) cyclonic and (right) anticyclonic.

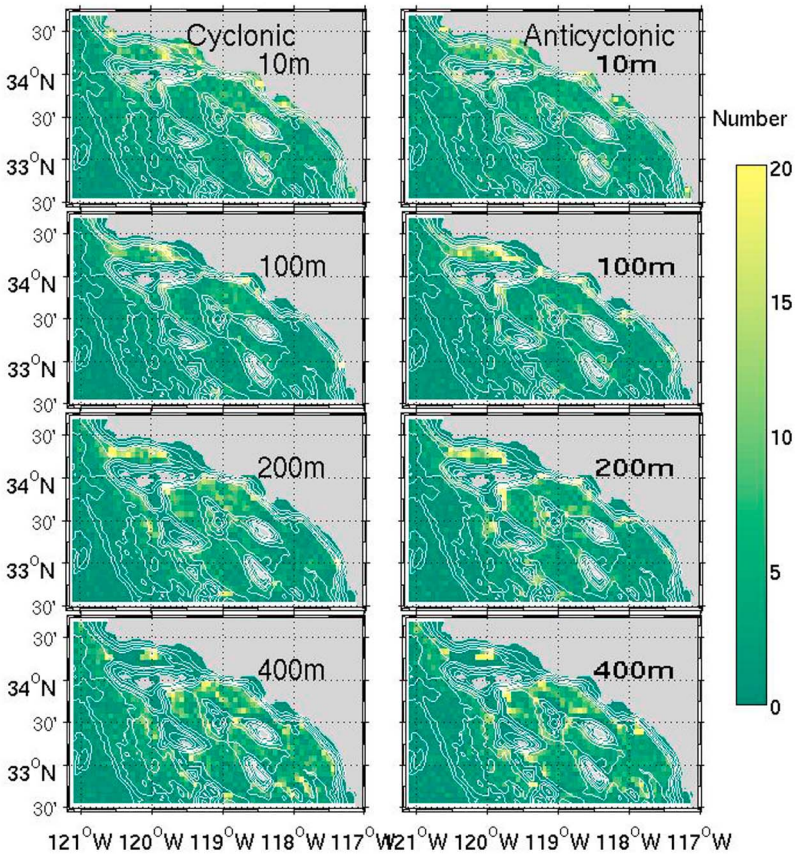

Figure 20. Same as Figure 18 but for eddy termination number inside the domain.

radial and tangential velocities respectively, and the first term is the pressure gradient, the second term is Coriolis acceleration and terms in parentheses denote the nonlinear effect. For an eddy in which the first two terms are dominant, the eddy is in geostrophic balance; if the terms in the parentheses cannot be neglected, the eddy is in ageostrophic balance when the local Rossby number is a finite value. To exclude the effect of the surface wind stress curl, two eddies at 50 m are plotted in Figure 21 as examples: the one with a mesoscale size is in geostrophic balance and another with submesoscale size is in ageostrophic balance.

[41] The twelve-year numerical product shows that most of eddies are in geostrophic balance, but some submesoscale eddies are ageostrophic balance because local Rossby numbers are in finite values. Figure 22 shows a scattering figure that characterize the relationship between eddy size and relative vorticity normalized by the planet vorticity, i.e., Rossby number. Actually, when the tangential velocity of an eddy is in a scale of 0.2 m/s, and its size is 10 km, its local Rossby number (normalized relative vorticity, see Figures 10 and 11) at 34°N is about 0.5. When an eddy size is less than 10 km (the first baroclinic deformation radius in the SCB is about 20–30 km [*Dong and McWilliams*, 2007]), the eddy can considered as a submesoscale eddy. Most of eddies with their sizes larger than 10 km have Rossby numbers smaller than 0.5 and they are in a good geostrophic balance. With their sizes smaller than 10 km, some of them have finite Rossby numbers around one unit but some of them still hold good geostrophic relationship with Rossby number smaller than 0.5.

6.3. Summary

[42] Oceanic circulation in the SCB is characterized by multiple-scale variations due to the complexity in the bottom topography, coastline and wind stress curls as well [*Dong et al.*, 2009a]. Using twelve years (1996–2007) high-resolution (1 km) numerical products of an oceanic circulation model in the SCB, which has been verified by previous studies, we investigate eddy variations in the SCB. First of all, an eddy data set on nine vertical levels is developed using a velocity geometry-based automated eddy detection scheme. Statistical analysis applied to the eddy data set reveals statistical characteristics of three-dimensional eddies in the SCB, including vertical and horizontal distribution of eddy parameters, such as, sizes, relative vorticity and lifetime. These eddy generation data have indicated that the dominant eddy generation mechanism in the SCB is likely caused by the presence of islands and headlands: horizontal shearing of oceanic flow-passing islands and headlands, wind stress curls due to islands, fronts and unevenly distributed bottom stresses and bottom fronts due to shelf slopes around islands. The seasonal and interannual eddy variations show that anticyclonic eddies have the largest numbers during the season of fall. The sandwiched vertical structure shows that the stratification present a barrier for

eddies from either the surface or the bottom. Based on the three-dimensional numerical product, we develop a method to extract information on the vertical structure of eddies, which shows that there are three types of eddies in terms of vertical shape: bowl-shaped, lens-shaped and cone-shaped. The dynamical analyses show that most submesoscale eddies in the SCB are in ageostrophic balance whereas most mesoscale eddies are in geostrophic balance.

[43] In a downscaling model, eddies remotely generated have been filtered along open boundaries. Though eddies tend to move westward and such filtering might have minor effects on the eddies in the SCB, we limits our studies to eddies which are generated and die inside the domain. Mesoscale and submesoscale eddy observational data are very scarce, especially sub-surface data, therefore the three-dimensional eddy characteristics presented in this study from a numerical product have yet to be verified by more observational investigations.

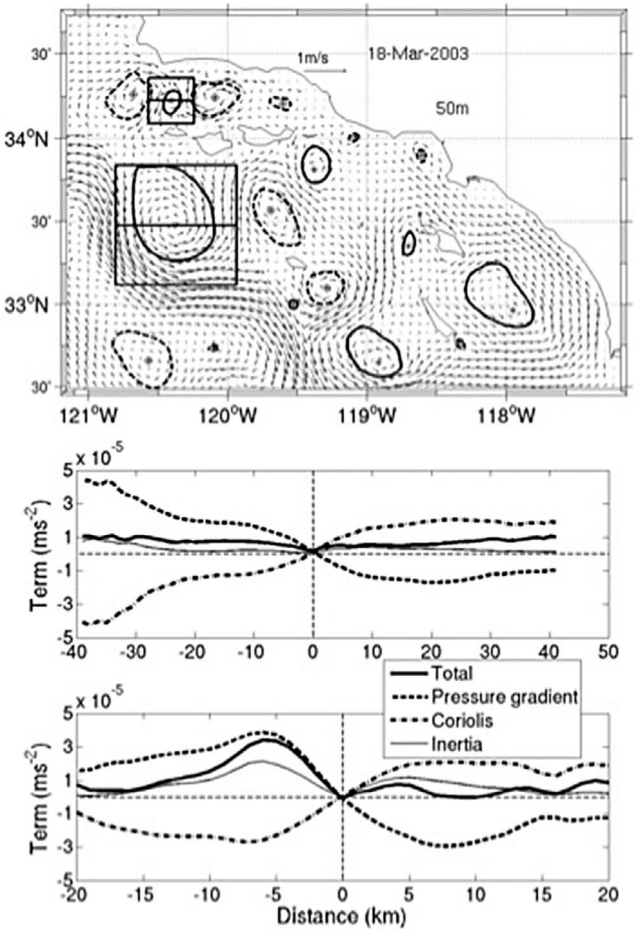

Figure 21. Two examples show geostrophic and ageostrophic balanced eddies at a level of 50 m. Top plot is a snapshot of currents at 50 m. The solid (dashed) circle-like lines are cyclonic (anticyclonic) eddies' boundaries. The stars are eddy centers. The two eddies are highlighted for dynamical balance analysis. Middle and bottom plots are dynamical balance analysis for the larger eddy and smaller eddy, respectively.

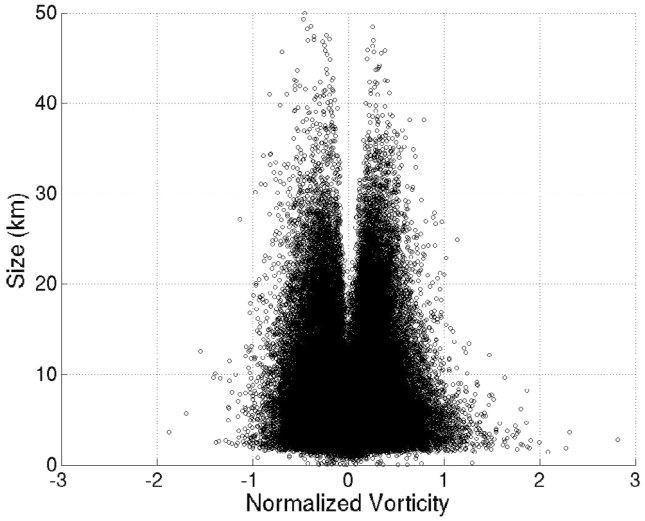

Figure 22. The normalized relative vorticity of eddies versus eddy sizes.

[44] **Acknowledgments.** C.D. appreciates the support from his NASA grant NNX08AI84G and ONR grant N00014-10-1-0564. C.D. is also supported by a visiting scholar grant from State Key Laboratory of Satellite Ocean Environment Dynamics, China. X.L., Y.L., and Y.P.G. are grateful for support from the Knowledge Innovation Program of the Chinese Academy of Sciences (grant KZCX1-YW-12-4) and National Basic Research Program of China (2007CB411801). D.C. is supported by research grants from Ministry of Science and Technology (2008GR1335,2007CB816005) and National Science Foundation of China (40730843). T.D. acknowledges support from ONR RaDyO contract N00014-07-1-0732 and grant N000140811178 for his ONR Secretary of the Navy/Chief of Naval Operations Chair in Oceanographic Sciences for Francesco Nencioli, Songnian Jiang, Derek Manov, and himself. Y.P.G. thanks Joint Institute for Regional Earth System of UCLA for the host of Y.P.G.'s visit at UCLA. All authors thank Chunyan Li for his comments, which help improve the manuscript. Resources supporting this work were provided by the NASA High-End Computing (HEC) Program through the NASA Advanced Supercomputing (NAS) Division at Ames Research Center. Y.C. acknowledges support from the NOAA Integrated Ocean Observing System (IOOS) program through the Southern California Coastal Ocean Observing System (SCCOOS). This study was carried out in part by the Jet Propulsion Laboratory, California Institute of Technology, under a contract with NASA. We thank two anonymous reviewers for their comments.

References

Beckenbach, E., and L. Washburn (2004), Low-frequency waves in the Santa Barbara Channel observed by high-frequency radar, *J. Geophys. Res.*, *109*, C02010, doi:10.1029/2003JC001999.

Bray, N. A., A. Keyes, and W. M. L. Morawitz (1999), The California Current system in the Southern California Bight and the Santa Barbara Channel, *J. Geophys. Res.*, *104*(C4), 7695–7714, doi:10.1029/1998JC900038.

Caldeira, R. M. A., P. Marchesiello, N. P. Nezlin, P. M. DiGiacomo, and J. C. McWilliams (2005), Island wakes in the Southern California Bight, *J. Geophys. Res.*, *110*, C11012, doi:10.1029/2004JC002675.

Carton, J. A., G. Chepurin, X. Cao, and B. Giese (2000a), A simple ocean data assimilation analysis of the global upper ocean 1950–95: Part I. Methodology, *J. Phys. Oceanogr.*, *30*, 294–309, doi:10.1175/1520-0485(2000)030<0294:ASODAA>2.0.CO;2.

Carton, J. A., G. Chepurin, and X. Cao (2000b), A simple ocean data assimilation analysis of the global upper ocean 1950–95: Part II. Results, *J. Phys. Oceanogr.*, *30*, 311–326, doi:10.1175/1520-0485(2000)030<0311:ASODAA>2.0.CO;2.

Carton, X. (2001), Hydrodynamical modeling of oceanic vortices, *Surv. Geophys.*, *22*, 179–263, doi:10.1023/A:1013779219578.

Chelton, D. B., et al. (2011), Global observations of nonlinear mesoscale eddies, *Prog. Oceanogr.*, *91*, 167–216, doi:10.1016/j.pocean.2011.01.002.

Dever, E. P., M. C. Hendershott, and C. D. Winant (1998), Statistical aspects of surface drifter observations of circulation in the Santa Barbara Channel, *J. Geophys. Res.*, *103*(C11), 24,781–24,797, doi:10.1029/98JC02403.

Dickey, T. D., F. Nencioli, V. S. Kuwahara, C. Leonard, W. Black, Y. M. Rii, R. R. Bidigare, and Q. Zhang (2008), Physical and bio-optical observations of oceanic cyclones west of the island of Hawai'i, *Deep Sea Res., Part II*, *55*(10–13), 1195–1217, doi:10.1016/j.dsr2.2008.01.006.

DiGiacomo, P. M., and B. Holt (2001), Satellite observations of small coastal ocean eddies in the Southern California Bight, *J. Geophys. Res.*, *106*, 22,521–22,543, doi:10.1029/2000JC000728.

Di Lorenzo, E. (2003), Seasonal dynamics of the surface circulation in the Southern California Current System, *Deep Sea Res., Part II*, *50*, 2371–2388, doi:10.1016/S0967-0645(03)00125-5.

Dong, C., and J. C. McWilliams (2007), A numerical study of island wakes in the Southern California Bight, *Cont. Shelf Res.*, *27*, 1233–1248, doi:10.1016/j.csr.2007.01.016.

Dong, C., and L.-Y. Oey (2005), Sensitivity of coastal currents near Point Conception to forcing by three different winds: ECMWF, COAMPS, and Blended SSM/I-ECMWF-Buoy winds, *J. Phys. Oceanogr.*, *35*, 1229–1244, doi:10.1175/JPO2751.1.

Dong, C., E. Idica, and J. McWilliams (2009a), Circulation and multiple-scale variability in Southern California Bight, *Prog. Oceanogr.*, *82*, 168–190, doi:10.1016/j.pocean.2009.07.005.

Dong, C., T. Mavor, F. Nencioli, S. Jiang, Y. Uchiyama, J. C. McWilliams, T. Dickey, M. Ondrusek, H. Zhang, and D. K. Clark (2009b), An oceanic cyclonic eddy on the lee side of Lanai Island, Hawai'i, *J. Geophys. Res.*, *114*, C10008, doi:10.1029/2009JC005346.

Dong, C., J. C. McWilliams, A. Hall, and M. Hughes (2011), Numerical simulation of a synoptic event in the Southern California Bight, *J. Geophys. Res.*, *116*, C05018, doi:10.1029/2010JC006578.

Grell, G. A., J. Dudhia, and D. R. Stauffer (1995), A description of the fifth-generation Penn State/NCAR mesoscale model (MM5), *Tech. Note NCAR/TN-398+STR*, Natl. Cent. for Atmos. Res., Boulder, Colo.

Harms, S., and C. D. Winant (1998), Characteristic patterns of the circulation in the Santa Barbara Channel, *J. Geophys. Res.*, *103*(C2), 3041–3065, doi:10.1029/97JC02393.

Hickey, B. M. (1979), The California Current System—Hypotheses and facts, *Prog. Oceanogr.*, *8*, 191–279, doi:10.1016/0079-6611(79)90002-8.

Hickey, B. M. (1998), Coastal oceanography of western North America from the tip of Baja California to Vancouver Island, in *The Sea*, vol. 11, edited by A. Robinson and K. Brink, pp. 345–393, John Wiley, New York.

Hickey, B. M., E. L. Dobbins, and S. E. Allen (2003), Local and remote forcing of currents and temperature in the central Southern California Bight, *J. Geophys. Res.*, *108*(C3), 3081, doi:10.1029/2000JC000313.

Hwang, C., C.-R. Wu, and R. Kao (2004), TOPEX/Poseidon observations of mesoscale eddies over the Subtropical Countercurrent: Kinematic characteristics of an anticyclonic eddy and a cyclonic eddy, *J. Geophys. Res.*, *109*, C08013, doi:10.1029/2003JC002026.

Kim, S. (2010), Observations of submesoscale eddies using high-frequency radar-derived kinematic and dynamic quantities, *Cont. Shelf Res.*, *30*, 1639–1655, doi:10.1016/j.csr.2010.06.011.

Large, W. G., J. C. McWilliams, and S. C. Doney (1994), Oceanic vertical mixing: A review and a model with a nonlocal boundary layer parameterization, *Rev. Geophys.*, *32*, 363–403, doi:10.1029/94RG01872.

Lynn, R. J., and J. J. Simpson (1987), The California Current system: The seasonal variability of its physical characteristics, *J. Geophys. Res.*, *92*(C12), 12,947–12,966, doi:10.1029/JC092iC12p12947.

Lynn, R. J., and J. J. Simpson (1990), The flow of the undercurrent over the continental borderland off southern California, *J. Geophys. Res.*, *95*(C8), 12,995–13,008, doi:10.1029/JC095iC08p12995.

McWilliams, J. C., and G. R. Flierl (1979), On the evolution of isolated non-linear vortices, *J. Phys. Oceanogr.*, *9*, 1155–1182, doi:10.1175/1520-0485(1979)009<1155:OTEOIN>2.0.CO;2.

Mitarai, S., D. A. Siegel, J. R. Watson, C. Dong, and J. C. McWilliams (2009), Quantifying connectivity in the coastal ocean with application to the Southern California Bight, *J. Geophys. Res.*, *114*, C10026, doi:10.1029/2008JC005166.

Nencioli, F., C. Dong, T. Dickey, L. Washburn, and J. McWilliams (2010), A vector geometry based eddy detection algorithm and its application to high-resolution numerical model products and high-frequency radar surface velocities in the Southern California Bight, *J. Atmos. Oceanic Technol.*, *27*, 564–579, doi:10.11.1175/2009JTECHO725.1.

Oey, L.-Y. (1999), A forcing mechanism for the poleward flow off the southern California coast, *J. Geophys. Res.*, *104*(C6), 13,529–13,539, doi:10.1029/1999JC900066.

Oey, L.-Y., C. Winant, E. Dever, W. Johnson, and D.-P. Wang (2004), A model of the near surface circulation of the Santa Barbara Channel: Comparison with observations and dynamical interpretations, *J. Phys. Oceanogr.*, *34*, 23–43, doi:10.1175/1520-0485(2004)034<0023:AMOTNC>2.0.CO;2.

Ohlmann, J. C., and S. Mitarai (2010), Lagrangian assessment of simulated surface 565 current dispersion in the coastal ocean, *Geophys. Res. Lett.*, *37*, L17602, doi:10.1029/2010GL044436.

Schwartzlose, R. A. (1963), Nearshore currents of the western United States and Baja California as measured by drift bottles, California Cooperative Oceanic Fisheries Investigation Reports, vol. 9, 1 July 1960 to 30 June 1962, Mar. Res. Comm., Calif. Dep. of Fish and Game, Sacramento.

Shchepetkin, A. F., and J. C. McWilliams (2005), The Regional Oceanic Modeling System (ROMS): A split-explicit, free-surface, topography-following-coordinate oceanic model, *Ocean Modell.*, *9*, 347–404, doi:10.1016/j.ocemod.2004.08.002.

Watson, J., S. Mitarai, D. Siegel, J. E. Caselle, C. Dong, and J. McWilliams (2010), Realized and potential laval connectivity in the Southern California Bight, *Mar. Ecol. Prog. Ser.*, *401*, 31–48, doi:10.3354/meps08376.

Watson, J. R., C. G. Hays, P. T. Raimondi, S. Mitarai, C. Dong, J. C. McWilliams, C. A. Blanchette, J. E. Caselle, and D. A. Siegel (2011), Currents connecting communities: Nearshore community similarity and ocean circulation, *Ecology*, *92*, 1193–1200, doi:10.1890/10-1436.1.

Winant, C. D., and C. E. Dorman (1997), Seasonal patterns of surface wind stress and heat flux over the Southern California Bight, *J. Geophys. Res.*, *102*(C3), 5641–5653, doi:10.1029/96JC02801.

Y. Chao, NASA Jet Propulsion Laboratory, California Institute of Technology, 4800 Oak Grove Rd., Pasadena, CA 91109, USA.

D. Chen, State Key Laboratory of Satellite Oceanic Environment Dynamics, SIO/SOA, 36 N. Baochu Rd., Hangzhou, 310012, China.

T. Dickey, Department of Geography, University of California, 552 University Rd., Santa Barbara, CA 93106, USA.

C. Dong and J. C. McWilliams, Institute of Geophysics and Planetary Physics, University of California, 405 Hilgard Ave., Los Angeles, CA 90095, USA. (cdong@atmos.ucla.edu)

Y. Guan, X. Lin, and Y. Liu, State Key Laboratory of Tropical Oceanography, South China Sea Institute of Oceanology, 164 W. Xingang Rd., Chinese Academy of Sciences, Guangzhou 510301, China.

F. Nencioli, Laboratoire d'Océanographie Physique et Biogéochimique, UMR-CNRS-IRD 6535, Centre d'Océanologie de Marseille, Université de la Méditerranée, F-13288 Marseille, Cedex 9, France.